Investigation of Physical Phenomena Underlying Temporal-Enhanced Ultrasound as a New Diagnostic Imaging Technique: Theory and Simulations

Sharareh Bayat, Shekoofeh Azizi, Mohammad I. Daoud, Guy Nir, Farhad Imani, Carlos D. Gerardo, Pingkun Yan, Amir Tahmasebi, Francois Vignon, Samira Sojoudi, Storey Wilson, Kenneth A. Iczkowski, M. Scott Lucia, Larry Goldenberg, Septimiu E. Salcudean, Purang Abolmaesumi, and Parvin Mousavi

***Abstract*— Temporal-enhanced ultrasound (TeUS) is a novel noninvasive imaging paradigm that captures information from a temporal sequence of backscattered US radio frequency data obtained from a fixed tissue location. This technology has been shown to be effective for classification of various *in vivo* and *ex vivo* tissue types including prostate cancer from benign tissue. Our previous studies have indicated two primary phenomena that influence TeUS: 1) changes in tissue temperature due to acoustic absorption and 2) micro vibrations of tissue due to physiological vibration. In this paper, first, a theoretical formulation for TeUS is presented. Next, a series of simulations are carried out to investigate micro vibration as a source of tissue characterizing information in TeUS. The simulations include finite element modeling of micro vibration in synthetic phantoms, followed by US image generation during TeUS imaging. The simulations are performed on two media, a sparse array of scatterers and a medium with pathology mimicking scatterers that match nuclei distribution extracted from a prostate digital pathology data set. Statistical analysis of the simulated TeUS data shows its ability to accurately classify tissue types. Our experiments suggest that TeUS can capture the microstructural differences, including scatterer density, in tissues as they react to micro vibrations.**

Manuscript received August 28, 2017; accepted December 13, 2017. Date of publication December 19, 2017; date of current version March 1, 2018. This work was supported in part by the Natural Sciences and Engineering Research Council of Canada and in part by Philips Research North America, Boston, MA, USA. The work of G. Nir was supported by Prostate Cancer Canada Post-Doctoral Research Fellowship Award PDF2016-1338. *(Purang Abolmaesumi and Parvin Mousavi contributed equally to this work.) (Corresponding authors: Purang Abolmaesumi; Parvin Mousavi.)*

S. Bayat, S. Azizi, F. Imani, C. D. Gerardo, S. Sojoudi, S. E. Salcudean, and P. Abolmaesumi are with the Department of Electrical and Computer Engineering, University of British Columbia, Vancouver, BC V6T 1Z4, Canada (e-mail: purang@ece.ubc.ca).

M. I. Daoud is with the Department of Computer Engineering, German Jordanian University, Amman 11180, Jordan.

G. Nir is with the Department of Urologic Sciences, University of British Columbia, Vancouver, BC V6T 1Z4, Canada.

P. Yan, A. Tahmasebi, and F. Vignon are with Philips Research North America, Cambridge, MA 02141 USA.

S. Wilson and M. S. Lucia are with the Department of Pathology, University of Colorado Anschutz Medical Campus, Aurora, CO 80045 USA.

K. A. Iczkowski is with the Medical College of Wisconsin, Milwaukee, WI 53226 USA.

L. Goldenberg is with the Vancouver Prostate Centre, Vancouver, BC V6T 1Z4, Canada.

P. Mousavi is with the School of Computing, Queen's University, Kingston, ON K7L 3N6, Canada (e-mail: pmousavi@cs.queensu.ca).

Digital Object Identifier 10.1109/TUFFC.2017.2785230

***Index Terms*— Finite element analysis, scatterer density, temporal-enhanced ultrasound (TeUS), tissue characterization, US simulations.**

I. Introduction

In THE past three decades, ultrasound (US) imaging has been increasingly used for tissue characterization and non-invasive detection of disease. Methods based on the analysis of US B-mode, radio frequency (RF), and Doppler data have been shown to correlate with tissue pathology [1]–[7]. These methods primarily rely on envelope statistics in B-mode data, the analysis of the power spectrum of RF data [8]–[10], or the shift in frequency spectrum of the backscattered RF data to estimate tissue types [4]. Viscoelastic properties of the tissue have also been estimated from RF data by compressing the tissue using acoustic radiation force or external mechanical stimuli, in elastography [11]–[16].

Our group has recently proposed a tissue characterization paradigm, referred to as *temporal-enhanced US* (TeUS), that utilizes machine learning approaches to extract information from a temporal sequence of RF data obtained from a stationary tissue location. TeUS data is captured following the sonication of the tissue over a short period of time while the probe is held stationary [17]–[19] (Fig. 1). This data, consisting of a sequence of RF US frames, has been shown to carry tissue characterizing information [17], [20]. By training a classifier on TeUS data obtained from tissue types of known properties, we characterize an unknown tissue type based on its TeUS data signature. The key differentiation between TeUS and prior work in tissue characterization is that the TeUS-based approach is performed on a sequence of RF data (acquired in a few seconds) without external mechanical excitation. This approach was effectively applied to detect prostate cancer [20]–[23], various animal tissue types [24], and ablated tissue [25].

TeUS has been successfully used for characterization of prostate cancer in *ex vivo* [20], [24] and *in vivo* [21]–[23], [26], [27] studies. The reported area under receiver operating characteristic curve (AUC) in these studies are between 0.76 and 0.93. A comparison of TeUS with the analysis of power spectrum of RF data for tissue characterization

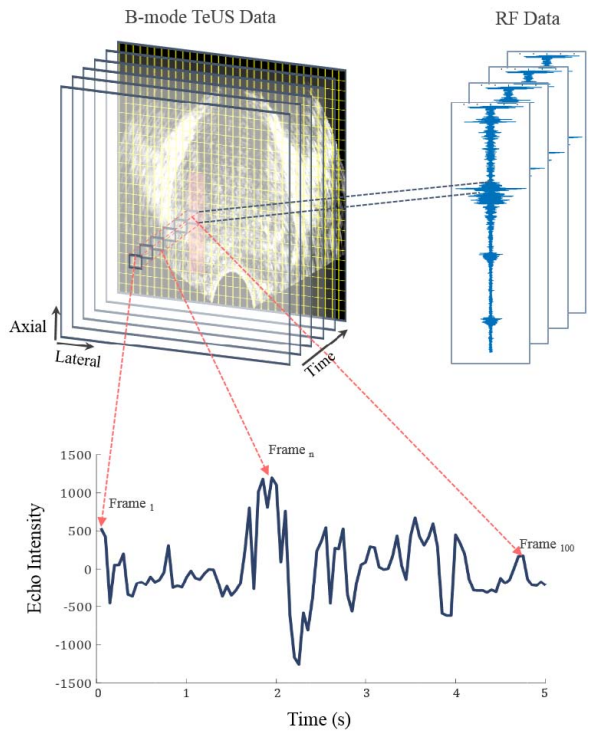

Fig. 1. TeUS data are generated from fixed tissue locations over a sequence of RF data frames. The time scale is a function of the frame rate. In our previous clinical data collections with a frame rate of 20 frames/s, the corresponding time for the caption of 100 frames is 5 s. Sample zero-mean time series of backscattered echo intensity (y-axis) from one fixed tissue location is shown (bottom), over a sequence of frames (x-axis).

showed that TeUS and RF spectral analysis complement each other [20], [22], with TeUS showing higher overall AUC. TeUS has also been used to distinguish various cancer grades in the preliminary whole-mount studies [28]. Our group has also proposed a cancer grading approach for transrectal ultrasound-guided prostate biopsy based on the analysis of *in vivo* TeUS data [29], [30]. The work in [29] demonstrated promising results to classify lower and higher grade prostate cancer with limited cancerous training samples, using TeUS.

To optimize TeUS for clinical translation, we aim to investigate the physical processes that govern US-tissue interaction during the acquisition of TeUS data [24]. Our efforts have focused on examining the two phenomena: 1) temporal accumulation of US-induced thermal effects as a result of acoustic absorption and 2) displacement due to micro vibrations in the tissue induced by physiological sources. We previously investigated changes in tissue temperature during TeUS data acquisition, using a numerical model [31]. The results demonstrated that changes in tissue temperature, which affect the speed of sound, can be used for tissue characterization. However, even with exaggerated image settings of high frame rate and acoustic power that do not match clinical imaging conditions, classification results were substantially below those achieved in our *ex vivo* and *in vivo* studies [31].

In this paper, we investigate the second phenomenon related to tissue micro vibrations as the main source of the tissue typing capabilities of TeUS with clinical image settings. Possible sources of tissue micro vibration include external, low-amplitude environmental vibrations, and internal physiological motion such as pulsation due to heartbeat [32], [33]. We build an extensive framework to simulate the interaction of TeUS with tissue and correlate micro vibrations induced in tissue microanatomy with the tissue characterization capability of TeUS.

To simulate US backscattering in tissue, abstractions are made about the mechanical and morphological properties of cells. Hunt *et al.* [34] provided a model in which the cell nuclei are simulated by point scatterers. More recently, Vlad *et al.* [35] investigated the three different cell types, scanned at frequencies of 10–30 MHz, and concluded that changes in US backscatter were directly related to morphological and nuclear changes in cells and those associated with cell death. Other studies also point to the important role of the cell's nucleus and its configuration in the formation of US backscatter, in addition to cellular morphology [36], [37].

Hunt *et al.* [38] studied the correlation between the spatial distribution of scattering points, which represent cell nuclei and US backscattering intensity. Baddour *et al.* [39] successfully measured US backscattering from individual cells *in vitro*. Their study proposed a model to describe the acoustic scattering of an individual cell, where the nucleolus (a body within the nucleus) was represented as a spherical scatterer with uniform mechanical properties. Previous literature have also suggested that the nuclei of cells are the prominent scattering sources of US [34], [40], [41]. Other studies have focused on modeling groups of cells. Specifically, they have demonstrated that subtle changes in morphological and spatial arrangement of nuclei can affect US backscattering dramatically [34], [42]–[44]. Oelze *et al.* [37] have indicated that acoustic estimation of the effective scattering sources of US is correlated to the size of cellular structures seen in matching light microscopic images of the tissue. Saha and Kolios [45] simulated a 2-D model to represent the effects of spatial organization and distribution of nuclei in cell aggregates on US backscatter. In their work, the nuclei were considered as weak scatterters. More recently, ultrasonic backscatter coefficient (BSC) measurements were performed on biophantoms with different cell concentrations [46]. The findings showed that in two of the phantoms where most of the cell volume was occupied by the cytoplasm, the whole cell played a major role in the BSC behavior. Han and O'Brien [47] suggested that a structure function was required for accurately modeling the acoustic scattering in dense medium. In their work, the centers of the nuclei were used to represent the location of scatterers.

In this paper, we present a scattering model to investigate the physiological processes that contribute to tissue characterizing capabilities of TeUS. Our model is based on the findings of previous studies [34], [39]–[41], where cellular structures, particularly nuclei, are hypothesized to be a main scattering source of US. Specifically, we expand on the previous work of [38] in the context of TeUS. We combine finite element modeling (FEM) and US simulation using Field II [48] to model the effect of micro vibration of nuclei, as a result of external or physiological vibration, on the backscattered TeUS data. The results of our study suggest that the micromotions are the main source of the tissue characterization

capabilities of TeUS. Using digital pathology data from the prostate of 10 patients, and the identified nuclei in these slides, we demonstrate that the TeUS analysis of simulated backscattered signals can effectively separate cancer and benign tissues. Furthermore, we analyze the effect of various parameters of simulation such as the US vibration, frequency, the distribution of nuclei and the elasticity of the medium on TeUS tissue characterization. Finally, we compare the performance of TeUS in simulated data with the analysis of the spectrum of a single RF frame similar to [49]. The remainder of this paper is organized as follows. Section II briefly overviews the theoretical background for US image formation in the context of TeUS data. Section III details the FEM and US simulations by providing the numerical formulations. The results of the simulations and tissue classification using TeUS are shown in Section IV. Results from the sensitivity analysis of the simulation parameters are also reported here. Finally, the discussion and summary of this paper are presented in Section V.

II. Theoretical Background

The characteristic model for the formulation of RF backscattered US signal can be expressed as [51], [52]

$$I(x) = P(x) * S(x) + n \tag{1}$$

where $P(x)$, US point spread function at an arbitrary point x, is convolved with $S(x)$, the tissue scattering function at the same point, to generate $I(x)$, the backscattered RF data at point (x). In this equation, n represents the random noise.

If we assume that $[S(x)]$ varies locally as a function of time, a simple model of this effect at point x_0 can be expressed as $S(x_0 + f(t))$, where $f(t)$ is a time-varying function and t is the "slow time" (i.e., frame number). For relatively small $f(t)$, the first-order approximation of Taylor expansion of S can be written as

$$S(x_0 + f(t)) = S(x_0) + \frac{\partial S(x)}{\partial x}\bigg|_{x=x_0} f(t) \tag{2}$$

where $(\partial S/\partial x)(x_0)$ is the local change in the scattering function about point x_0. As stated in Section I, we previously investigated a scenario where variations in $f(t)$ were primarily due to induced thermal effects as a result of acoustic absorption [31]. In this paper, we investigate an alternative hypothesis, where variations in $f(t)$ are a result of tissue micro vibrations due to physiological vibration. Let $f(t)$ be a sinusoidal function of the form

$$f(t) = a(x_0)\ \sin(\omega t) \tag{3}$$

where $a(x_0)$ is the amplitude of the micro vibration at point x_0, and ω is the frequency of vibration. In a fully elastic tissue, $a(x_0)$ is inversely proportional to $E(\omega)$, the local elasticity, which is frequency dependent. In a viscoelastic medium, $a(x_0)$ is inversely proportional to a function of $E(\omega)$ and $\mu(\omega)$, where $\mu(\omega)$ is the local viscosity, which is also frequency dependent [52]. Equation (2) can be rewritten as

$$S(x_0 + a(x_0)\sin(\omega t)) = S(x_0) + a(x_0)\ \frac{\partial S(x)}{\partial x}\bigg|_{x=x_0} \sin(\omega t). \tag{4}$$

Combining (1) and (4), we have

$$I(x_0, t) = (P(x) * S(x))\Big|_{x=x_0} + a(x_0)(P(x) * \frac{\partial S(x)}{\partial x})\Big|_{x=x_0} \times \sin(\omega t) + n. \tag{5}$$

The first term of (5) corresponds to the time-invariant component of the RF signal received from point x_0. This component depends only on the spatial variations of the backscattering function across the propagation medium. It can be characterized using the conventional analysis of the RF spectrum and B-mode texture. The second term corresponds to the time-varying components of $I(x_0, t)$ affected by local variations in the backscattering function, in slow time. Such local variations represent changes in tissue structure, such as changes in nuclear configuration.

Two important observations can be made about the second term of this equation: 1) in media with the same mechanical properties E and μ, the spectral analysis of TeUS captures $(P(x)*(\partial S(x)/\partial x))|_{x=x_0}$, which is related to spatial variations in the scattering function. This property can be of benefit to characterize, e.g., tissue at early stage cancer, where changes in nuclei configuration could dominate changes in tissue property and 2) where there are changes in mechanical properties, $a(x_0)$, and the scattering function, S, or the vibration frequency, ω, TeUS captures a combined effect for tissue characterization.

In the remainder of this paper, through a series of simulations, we demonstrate that local changes in tissue properties, captured by $a(x_0)\ (P(x) * (\partial S(x)/\partial x))|_{x=x_0}$ using, e.g., Fourier transform of TeUS, are effective features for tissue characterization. Our simulations include media with synthetic array of scatterers of varying distances and pathology mimicking simulations based on whole-mount prostate digital histopathology data. These simulations confirm our observations from (5) that as a result of micro vibration in the medium, TeUS can differentiate tissue types with subtle variations in the arrangement of scatterers.

III. Materials and Methods

Our simulation approach consists of three main components: 1) mechanical modeling to compute scatterers micromotion; 2) US image formation to construct TeUS data reflected from scatterers following the mechanical modeling; and 3) feature extraction for tissue characterization.

US data frames acquired in the TeUS procedure quantify the temporal variations of the backscattered US signal from a stationary tissue. Specifically, if the source of these temporal variations is a sinusoidal physiological excitation, such as the heartbeat, the frequency analysis of the TeUS data should demonstrate a peak at the excitation frequency. In this paper, we use the amplitude of the power spectrum of TeUS data at the excitation frequency as a tissue characterization feature to differentiate tissue types.

The simulations are performed on two scattering media; the first is a medium with a synthetic, sparse array of scatterers and the second is a medium with pathology mimicking scatterers that match nuclei distribution extracted from a prostate digital pathology data set. The former data is used to establish a

basis for TeUS as a tissue characterization approach that can accurately capture subtle changes in a scattering medium. The latter data is used to mimic the prostate tissue behavior in response to induced micro vibrations, under controlled tissue mechanical properties. The simulation of the array of scatterers considers an ensemble array of point scatterers embedded in a $5 \times 5 \times 5$-cm^3 homogeneous phantom. The dimensions of this phantom are set so that it is beyond the US imaging depth we have used, and is consistent with our simulations based on histopathology slices to encapsulate the size of a large prostate. This is to ensure that we cover the whole imaging depth in each simulation, while physical boundaries of phantoms do not affect the simulated images. The phantom size is kept consistent across all simulations.

Spectral analysis of TeUS is then used to derive features for tissue characterization. The block diagram of the overall methodology is demonstrated in Fig. 2.

A. Simulation Design—Synthetic Array of Scatterers

In an attempt to simplify the recognition of the effect of the structural organization of scatterers on TeUS data, we perform simulations using an array of point scatterers. The objective is to demonstrate that subtle changes in scatterer distances at subacoustic wavelength scale can be detected by TeUS. Following the approach of Hunt *et al.* [38], where they introduce constrained changes to the arrangement of point scatterers, we design media with different scatterer distances and keep all mechanical parameters such as elasticity and viscosity constant. A low-amplitude, low-frequency external force is applied to media to mimic physiological motion resulting in micro vibrations of the tissue.

1) Mechanical Modeling: This simulation considers an ensemble array of point scatterers embedded in a $5 \times 5 \times 5$-cm^3 homogeneous phantom. An FEM is generated in COMSOL Multiphysics 5.2 (COMSOL Inc., Burlington, MA, USA) for this purpose. As mentioned above, to simulate scatterer micromotion, a mechanical vibration with a low-amplitude and low-frequency signal is used. We employ a sinusoidal signal that vibrates the inferior surface of the phantom at 2 Hz with a peak amplitude of 10 μm. The boundary conditions are defined such that the lateral boundaries are considered as fixed boundaries. We used a model with constrained randomization of scatterers, where we designed a synthetic linear array of point scatterer pairs that are embedded in the FEM. Scatterers are separated in depth such that each scatterer pair is placed 1 mm away from the next pair. The two scatterers in each pair are separated by a distance D_s in axial direction, which has a value smaller than the acoustic wavelength (λ). There are 80 scatterers in total representing 4 cm of depth. Considering the x, y, z positions, representing the axial, lateral, and elevation coordinates, respectively, of the first scatterer in the array as X_1, the second scatterer from the first pair is located at

$$X_i = X_1 + [D_s \ 0 \ 0]^T, \quad i = 2. \tag{6}$$

The positions of the subsequent scatterers for $i \in [3 \ \ 80]$ in the following pairs (p) for $p \in [2 \ \ 40]$ can be expressed as

$$X_i = \begin{cases} X_{i-2} + [D_g \ 0 \ 0]^T, & i = \text{odd} \\ X_{i-1} + [D_s \ 0 \ 0]^T, & i = \text{even} \end{cases} \tag{7}$$

where X_i determines the ith scatterer's x, y, z coordinates. D_s defines the distance that separates the two scatterers within each pair. In the simulations, the value of D_s is separately set to 5, 10, 20, and 40 μm and $D_g = 1$ mm is the fixed distance between adjacent pairs. The 1-mm distance between the scatterer pairs (D_g) is chosen to represent a spacing of approximately five times the US wavelength (233 μm). This will ensure that for the range of micro vibrations applied to the medium, the responses of all pairs are distinct from each other. This feature of our design allowed us to get insight into the phenomenon, not to model actual tissue structures.

D_g is fixed as 1 mm and D_s is set to 5, 10, 20, and 40 μm to simulate four different media with scattering pairs with distances well below the wavelength.

Mechanical simulations are then run with a time step of 5 ms, which corresponds to a sampling frequency of 200 frames/s. This sampling frequency is sufficient to capture physiological sources of vibration, such as the heartbeat. The simulation is run for 512 time steps, which is equivalent to 2.5 s. Fig. 3(a) illustrates the mechanical simulation setup.

2) Ultrasound Image Formation: US images are simulated using Field II [48]. The background sound speed is set to 1540 m/s, which is close to the speed of sound in soft tissue [53]. The center frequency of the probe is configured to be 6.6 MHz. Moreover, the number of active elements in the transmit and receive apertures are set to 40. Each element is set to have width of 279.8 μm, pitch of 304.8 μm, and height of 4 mm. The focal point is set to 2 cm. The computed US signals are recorded with a sampling frequency of 80 MHz.

To model the conventional US imaging of the FEM phantom, Field II is employed to synthesize US RF signals and generate a B-mode image of the phantom before applying the external vibration source, i.e., when the scatterers are located at their initial positions. Field II is also used to synthesize TeUS data by performing a sequence of 512 US simulations, such that each simulation corresponds to the spatial arrangement of the scatterers in the phantom generated during one of the time steps of the FEM model described in Section III-A-1. TeUS data for a given scatterer pair is generated by recording the RF signal that corresponds to the resolution cell including the pair, for all 512 US simulations. In this paper, the TeUs data that correspond to a 10-mm region centered on the focal point, containing nine scatterer pairs, are considered, as illustrated in Fig. 3(b). The nine middle scatterer pairs are chosen to represent a 10-mm region of interest (ROI) around the focal zone.

3) Feature Extraction: The methodology we employ for classification of media with different scatterer pair distances is based on the spectral analysis of TeUS data. To generate the TeUS power spectrum, we apply discrete Fourier transform (DFT) on the time series signal. The square of the second norm of the DFT is the power spectrum of the signal. The power spectrum is then averaged over the nine middle scatterer pairs for each scenario ($D_s = 5$, 10, 20, and 40 μm), while the mean values are removed. The nine middle scatterer pairs are chosen to consider the 10-mm ROI around the focal zone (2 cm). The average power spectrum amplitude of peaks at the vibration frequency is taken as the feature used for classification.

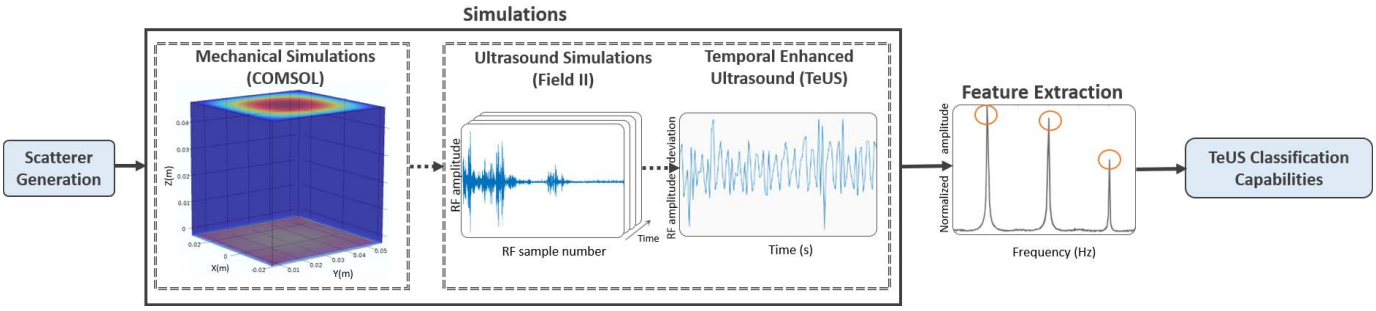

Fig. 2. Overall methodology: scatterer generation, US simulation, and feature extraction for tissue characterization. The temporal micro pulsations that vibrate the tissue are mechanically simulated in COMSOL Multiphysics. The resulting displaced scatterers are fed into the US simulation software Field II to generate TeUS data. Spectral analysis is used for feature extraction and tissue classification.

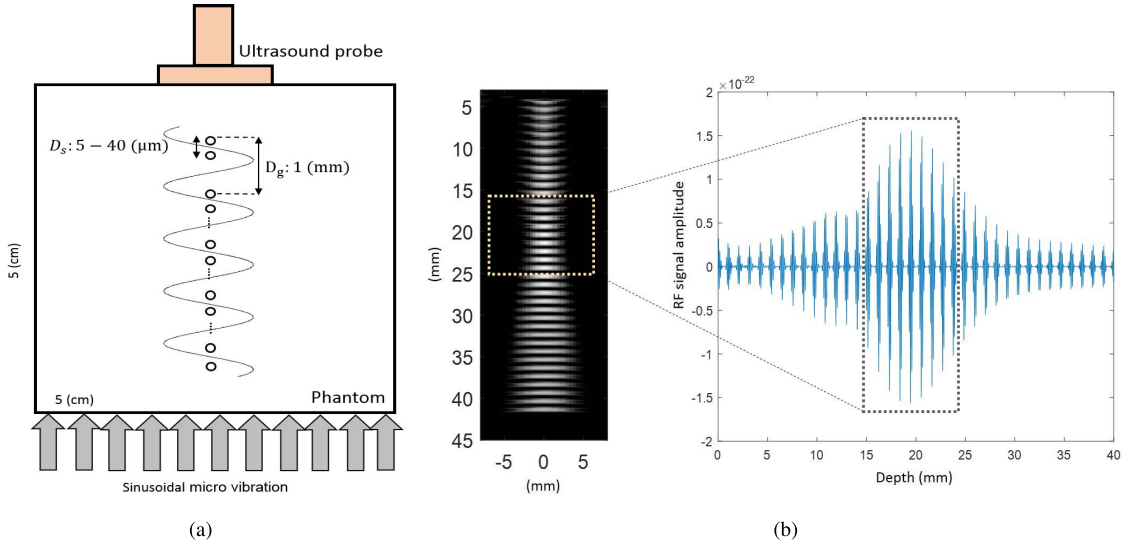

Fig. 3. Synthetic data structure, mechanical modeling, and TeUS simulations setup. (a) Mechanical modeling: pairs of scatterers are separated 1 mm apart from each other with interpair distances of 5, 10, 20, and 40 μm for various simulations. Sinusoidal micro vibrations are pulsating the inferior surface of the phantom to induce scatterer micromotion. The simulated transducer is placed on the top surface to generate US RF data. (b) RF response of each scatterer pair around the focal zone (10-mm region) are recorded as a function of time to generate TeUS data.

B. Simulation Design—Pathology Mimicking Scatterers

The second simulation setup uses pathology data from whole-mount prostate cross sections. In this simulation, we consider nuclei as a main source of scattering. We extract the positions of nuclei from a digital pathology data set, where the locations of cancerous cells are marked by an expert pathologist [54]. We divide the digitized slides to blocks of 2×2 mm^2, with a resolution of 0.5 μm/pixel.

1) Mechanical Modeling: Here, a single scattering point is considered at each nucleus location segmented from the pathology slides. A 2-D model based on the coordinates of these nuclei in slices parallel to the xz plane is generated for different benign and cancer regions. Fig. 4 illustrates the ROI selection process on a sample pathology slide used to determine the location of scatterers.

The computational model entails a $5 \times 5 \times 5$-cm^3 homogeneous linear viscoelastic phantom in which the elasticity is set to 25 kPa [52]. Viscosity is included in the simulations using Kelvin–Voigt model [55], to represent the absorption properties of the prostate tissue, and is set to 2.15 Pa.s [56]. To mimic the prostate tissue, we consider a near-incompressible material where the Poisson ratio is $\nu = 0.49$ [57]. The elasticity and viscosity values are considered as a part of the process to mechanically model the tissue in the FEM simulations. These parameters do not directly affect the modeling of US propagation in Field II simulations. We use the same external vibration source as in the synthetic array of scatterers (Section III-A1). The numerical calculations are performed for 2.5 s.

2) Ultrasound Image Formation: Using Field II, the first US image frame is generated based on the initial positions of scatterers. The settings for the sampling frequency, the probe frequency, and the focal point are same as those of the synthetic array of scatterers, set to 80 and 6.6 MHz and 2 cm, respectively. Fig. 5(a) and (b) illustrates a sample whole-mount histopathology slide and the corresponding Field II generated B-mode image, respectively.

We then generate the TeUS data using Field II for each of the ROIs. In all simulations, the location of scatterers is the same in the FEM simulation. Moreover, the ROI containing the scatterers is placed at the focal point for all Field II simulations.

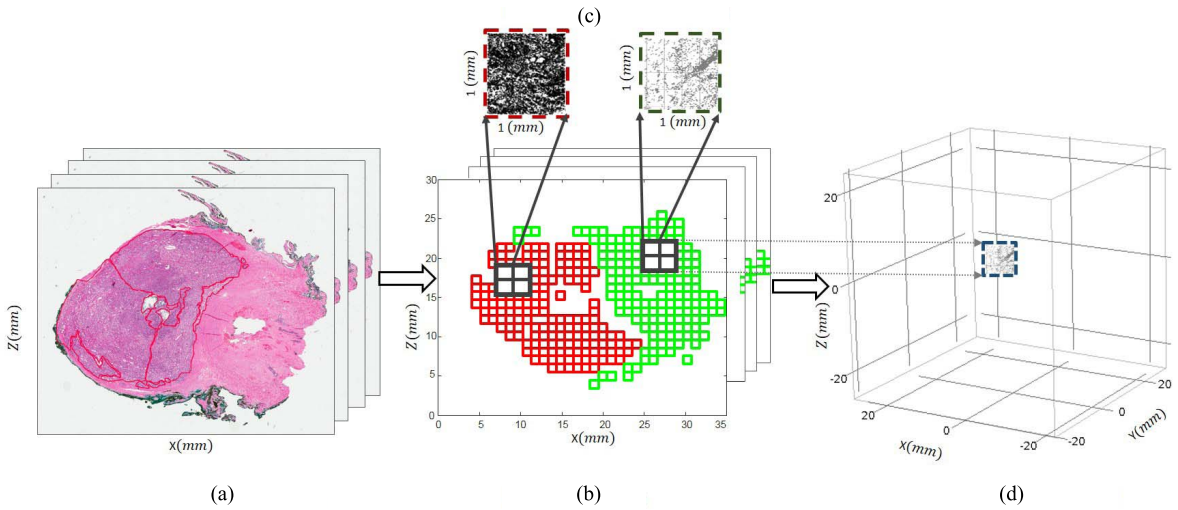

Fig. 4. ROI selection and nuclei-based scatterer generation process. (a) Sample of histopathology slide [54], where the red boundary depicts the cancer area. (b) Digitized slide overlaid on the histopathology slide, where green and red areas represent the benign and cancer regions, respectively. The selected ROIs are shown by black squares. (c) Extracted nuclei positions in the selected ROIs; a cancer region (left) and a benign region (right). (d) Extracted positions of nuclei from each ROI is embedded in an FEM model.

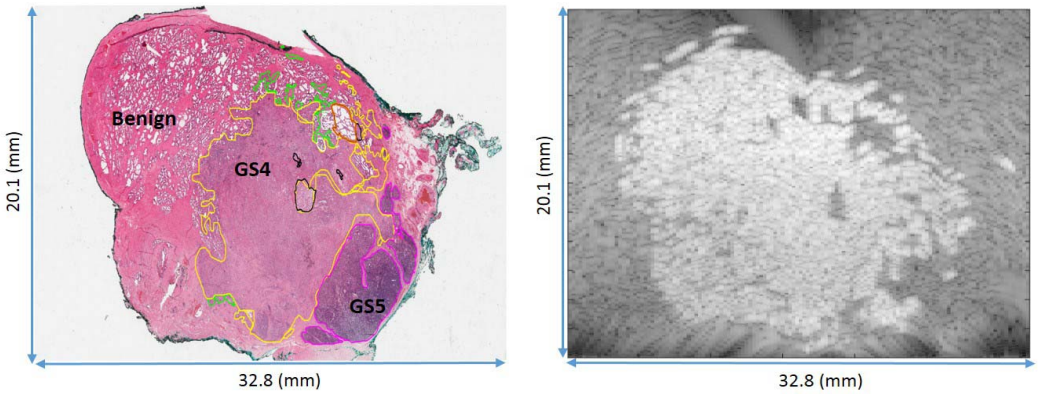

Fig. 5. (a) Sample whole-mount histopathology slide of the prostate. Different regions of cancer and benign tissues are shown in the pathology slide. (b) Corresponding simulated B-mode US image.

The simulated TeUS, containing the RF time series vector is stored as a set, denoted as RF_L^T, in which L is an $m \times n$ matrix, where $m = 229$ is the number of RF samples recorded in each RF scan line and $n = 18$ is the number of scan lines. T, the length of the TeUS data, is 512 frames. Therefore, each B-mode image is composed of 18 scan lines in the lateral direction and 229 samples in the axial direction. The 2×2 mm^2 regions in the synthesized B-mode images are subdivided into four ROIs. The ROI sizes are 1×1 mm^2. In total, we simulated 168 benign and cancer ROIs including 56 benign and 128 cancer ROIs form 14 histopathology slides of 10 patients.

3) TeUS Feature Extraction: To generate the TeUS power spectrum, we apply DFT on the time series signal. The square of the second norm of the DFT is the power spectrum of the signal. The power spectrum is then averaged over each ROI while the mean values are removed. The amplitude of spectrum peaks at the vibration frequency and its harmonics are identified. The power spectrum amplitudes of the peaks recorded at the vibration frequency are used as a feature to separate tissue types (F_1).

4) Features of Single RF Frame: Feleppa *et al.* [49] have shown that spectral features of a calibrated RF signal can be used for detection of cancer and benign tissues in the prostate. We compare differentiation of tissue using features of TeUS data with that of the spectral features of a single US RF frame. For this purpose, we simulate the calibration method in [49], which includes acquiring RF data reflected by a flat reflector embedded in water background.

The flat reflector is simulated by a dense linear distribution of 50 000 point scatterers positioned uniformly across a continuous flat surface. The reflector is axially located at the focus and laterally extends across the entire medium.

The calibration RF signals received from the medium is used to calculate the single US RF frame features, by subtracting its power spectrum from the average power spectrum of RF data in each ROI. In particular, a line is fit to the spectrum of the calibrated RF signal. The fit line is then used to extract three

spectral features, namely, the zero-frequency intercept (LF_I), average slope (LF_S), and midband value (LF_M) [20].

IV. Results

A. Synthetic Array of Scatterers

A sample B-mode image simulated from the synthetic array of scatterers is shown in Fig. 3(b). Fig. 6(a) depicts the power spectrum amplitude of the TeUS for scatterer pairs with different subpair distances (D_s) from 5 to 40 μm. Noticeable amplitude differences between the spectra are observed at 2 Hz, which are the first observed peak in the spectrum, matching the vibration frequency. For classification purpose, we consider the power spectrum peak amplitude at the vibration frequency as classification feature F_1. This feature represents the second term of (5) and is a function of $(P(x) * (\partial S(x)/\partial x)|_{x=x_0}$.

To compare, we also compute a feature representing the derivative of the first term of (5) by analyzing a single RF US data. We use the following property of convolution in this computation to relate this feature to F_1 computed from the second term of (5):

$$P(x) * \frac{\partial S(x)}{\partial x} = \frac{\partial (P(x) * S(x))}{\partial x} \tag{8}$$

and calculate the root mean square (rms) of gradient of the RF image as this feature (F_g). Fig. 6(b) illustrates the comparison between the normalized values of this feature against normalized F_1. Although the two features demonstrate a similar trend with respect to D_s, the steeper slope of F_1 leads to a more sensitive feature for classification.

B. Pathology Mimicking Scatterers

Fig. 7(a) depicts the distribution of feature F_1 extracted from the power spectrum of TeUS, compared across benign and cancer ROIs at 2-Hz vibration frequency. The distributions are statistically significantly different between benign and cancer ROIs ($p = 4.46e - 20$ using a paired t-test).

Similar to the synthetic array of scatterers, we compare F_1 to the rms of gradient of the first RF image in benign and cancer ROIs (F_g). Fig. 7(b) represents the distribution of F_g in the first frame. Although the difference between benign and cancer ROIs are still statistically significant ($p = 1.8e - 12$), the distribution of F_1 shows a more profound sensitivity for tissue classification with a much smaller p-value.

C. Features of Single Ultrasound RF Frame

The distribution of the three features extracted from a single RF frame are shown in Fig. 8, where each feature is normalized between 0 and 1. The distributions of LF_I and LF_M features are statistically significantly different between benign and cancer ROIs ($p < 0.01$ for LF_I and $p < 0.01$ for LF_M using a paired t-test). However, the distribution of LF_S fails to show statistically significant difference between the two tissue types ($p = 0.25$). These results agree with Feleppa's derivations [1], [8]. LF_I and LF_M are both dependent on scatterer concentration, which differs between benign and cancer tissue types. On the other hand, LF_S is dependent on the scatterer radius, which in our simplified simulation model is considered consistent among all tissue types.

D. Sensitivity Analysis

We study the effect of two simulation parameters on tissue classification. These are the vibration frequency of the external vibration source and the elasticity of the medium in pathology mimicking simulations.

1) Effect of Vibration Frequency: The pathology mimicking simulation in Section III-B is replicated for the 1-, 10-, and 20-Hz vibration frequencies to evaluate the classification characteristics of TeUS in a wider range of frequencies. This setting covers near the heartbeat frequencies (1.6 Hz on average) plus additional simulations at higher frequencies (10 and 20 Hz), while all other parameters including the mechanical vibration amplitude, medium elasticity, and viscosity are identical to the previous pathology mimicking simulations.

Fig. 9 depicts the distribution of features extracted from TeUS, compared across benign and cancer ROIs at three vibration frequencies of 1, 10, and 20 Hz (Peak-1). In Fig. 9(a)–(c), the distributions are statistically significantly different between benign and cancer ROIs (all $p < 0.001$ using a paired t-test).

2) Effect of the Elasticity of the Medium: We have repeated the pathology mimicking simulations using media with three elasticity values of 5, 15, and 25 kPa. The chosen elasticities represent the three different sample stiffness values of the tissues in the range of elasticities defined in [52] for benign and cancerous tissues. In these simulations, the elasticity values were intentionally chosen the same for benign and cancer tissues to eliminate the effect of elasticity difference. Such a simulation design enables us to evaluate the accuracy of TeUS for tissue classification irrespective of elasticity.

The frequency of the external vibration is set to 20 Hz and all other media and simulation parameters are maintained the same as in the previous simulations. Fig. 10 depicts the distribution of feature F_1 extracted from TeUS, compared across benign and cancer ROIs at the vibration frequency. The benign and cancer ROIs are statistically separable regardless of the elasticity of the media ($p < 0.001$ in a two tailed t-test). Moreover, as presented in (5), the amplitudes of the average power spectrum peaks are approximately (given the viscosity of the medium) inversely proportional to E as the elasticity of the medium increases from 5 to 25 kPa.

V. Discussion and Conclusion

In this paper, we studied the physical processes underlying the interaction of a temporal sequence of US RF frames with tissue. In particular, we investigated tissue micro vibrations as the dominant source of the tissue typing capabilities of TeUS at clinical imaging settings. To achieve this goal, we first presented theoretical derivations that relate changes in tissue properties to information derived from TeUS using spectral analysis. Next, we verified the theoretical derivations by performing simulations of the interaction of tissue with US, analyzed over a sequence of image frames. We used a simplified mechanical model of micro vibrations of tissue mimicking phantoms with embedded scatterers by representing cell nuclei as point scatterers.

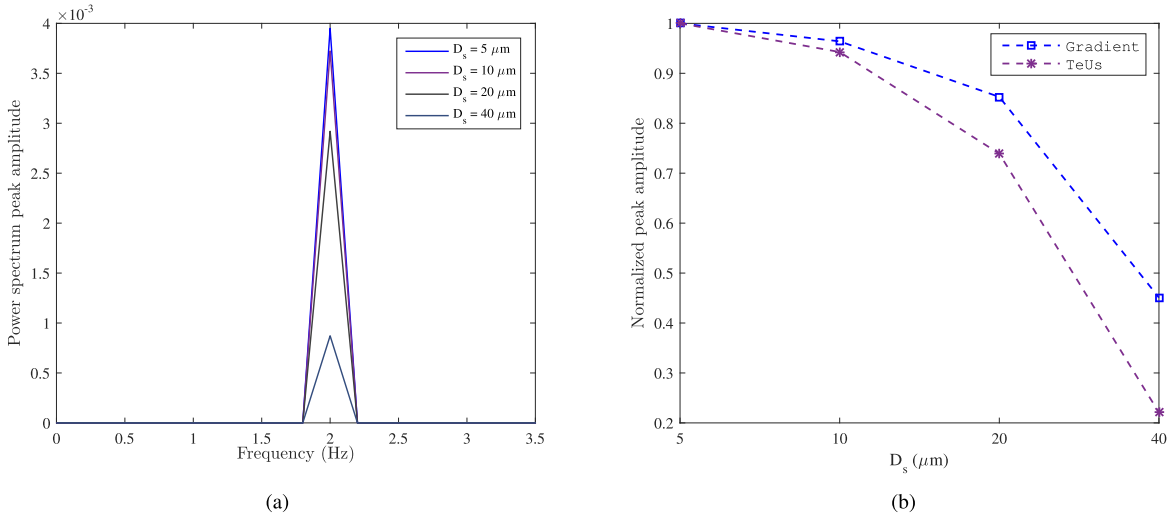

Fig. 6. (a) Spectral analysis of the synthetic array of scatterers. The amplitude of power spectrum at 2-Hz vibration frequency, computed in a 10-mm ROI centered at the focal point, is plotted versus D_s (not normalized). (b) Comparison between the normalized values of F_1 (normalized to the maximum value of F_1; purple dashed line) and F_g (blue dashed line) versus subpair distances (D_s) for synthetic array of scatterers.

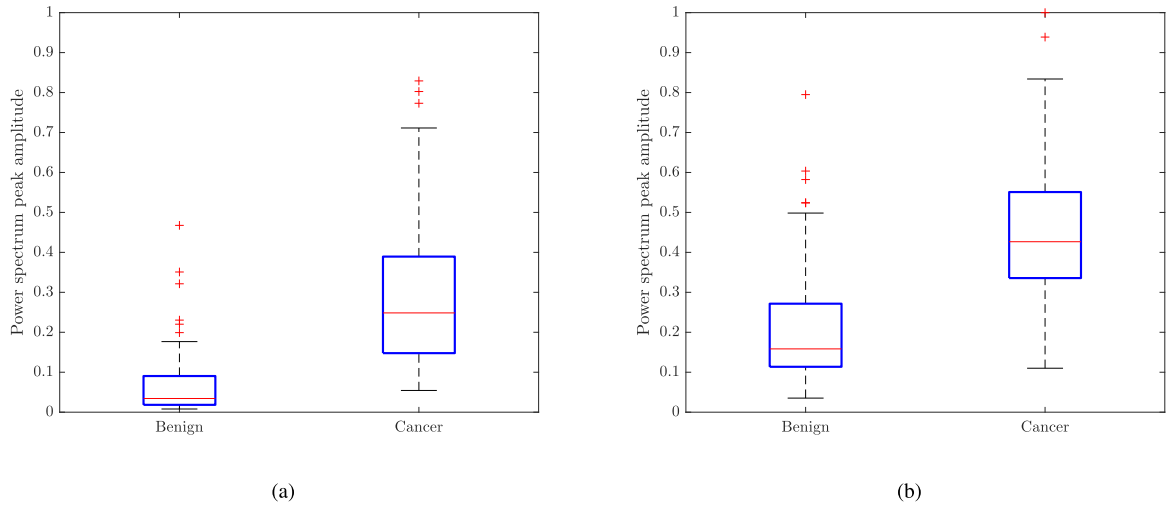

Fig. 7. (a) Distribution of the power spectrum peaks in the frequency spectrum of simulated TeUS data at the vibration frequency for the pathology mimicking data set. Median and standard deviations of the amplitudes of the peak (F_1) at 2 Hz for vibration frequency of 2 Hz. (b) Distribution of F_g in the first RF image frame.

In this paper, we considered the effect of introducing physical vibrations to the scatterers. The source of micro vibration was assumed to be a sinusoidal motion. In reality, such an assumption implies a periodic vibration with constant amplitude and frequency. Despite the fact that physiological processes can be better described using more complex functions with varying frequencies and amplitudes, the findings of our model can provide insight into the physiological processes that contribute to the tissue characterization capabilities of TeUS. Our future directions include the use of more complex functions, derived from our observations from *in vivo* data, to better describe the physiological vibrations that occur in tissue.

When an array of scatterers was embedded in a medium in pairs, at regular spacing between each pair, we observed that TeUS signatures were associated with the distances between the pairs (e.g., 5 and 10 μm). Results showed that TeUS is sensitive to scatterer arrangements and is able to differentiate between the pairs of various distances, even though these distances are substantially below the US wavelength. We estimated the second term of (5) from the spectral analysis of TeUS and analysis of the first backscattered RF image using gradient calculations. Results demonstrated that although the two approaches show a similar trend versus D_s, the TeUS-based analysis is much more sensitive to changes in the scattering function.

In the pathology mimicking simulation, we placed scatterers in phantoms according to distributions of nuclei in cancer and benign tissues. While in this paper, we modeled the nuclei as a major scattering source, other parts of the cell might also contribute to US scattering [37]. An extension of this paper may include a more elaborate US simulation framework that

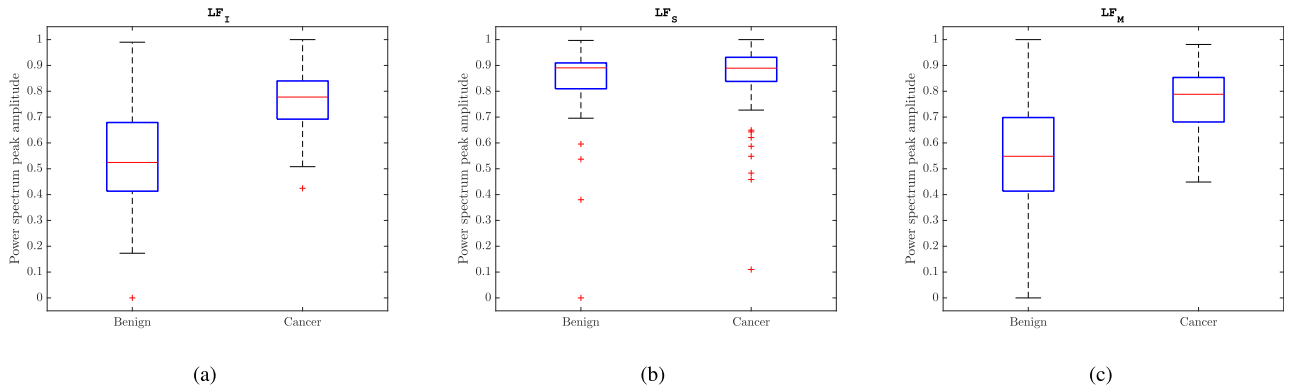

Fig. 8. Distribution of the three features extracted from a single RF frame among benign and cancer regions. (a) Intercept extrapolated to zero frequency (LF_I). (b) Slope of regression line fit to the spectrum (LF_S). (c) Midband value (LF_M).

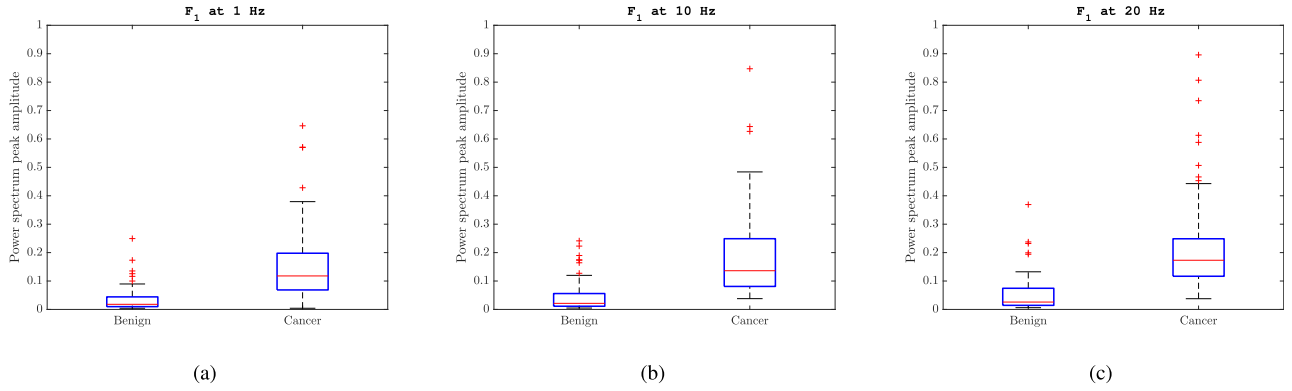

Fig. 9. Distribution of the peaks in the frequency spectrum of simulated TeUS data for the pathology mimicking data set. Median and standard deviations of the amplitudes of the peak (F_1) at (a) 1 Hz for excitation vibration frequency of 1 Hz, (b) 10 Hz and for vibration frequency of 10 Hz, and (c) 20 Hz and for excitation vibration frequency of 20 Hz.

considers other sources of scattering in tissue. We anticipate that the findings of this paper remain unchanged, irrespective of the dominant scattering source.

In our simulations, we showed statistically significant differences in the TeUS signatures of different tissue types. This is likely due to the changes in the backscattered US data that are dependent on tissue microstructure and that can be revealed as a result of micro vibration. We were able to differentiate tissue types at various mechanical vibration frequencies from 1 to 20 Hz. Similar to the synthetic array of scatterers, TeUS-based analysis also showed significantly higher sensitivity to separate benign and cancer ROIs compared with the analysis of the first backscattered RF image, when estimating the second term of (5) using gradient calculations.

In our previous *in vivo* experiments [21], [23], [58], we observed that low-frequency components (1–2 Hz) of TeUS provide the most discriminating features for distinguishing among Gleason patterns 3, 4, and benign tissue samples. Specifically for the prostate, this frequency range can be related to the pulsation of the vessels surrounding the tissue, which is at the heartbeat frequency. Therefore, the simulation frequencies are selected to represent relatively realistic scenarios. The 1 and 2 Hz are picked as near-heart rate ranges. We also used 10 and 20 Hz to demonstrate that our derivations can be generalized to other frequency ranges.

The findings of our simulations suggest that TeUS can take advantage of tissue micro vibration induced by physiological sources, such as the heartbeat or other internal and external vibrations, for tissue characterization. The timescale of data acquisition for TeUS analysis is approximately 2–5 s. Therefore, bulk tissue motion (e.g., bowel movement) that occur over timescales, that are too long (tens of seconds to minutes) to affect the TeUS measurements, is not considered as possible driving forces for the micro motion of scatterers. Rather as observed in our previous studies [33], the near the heartbeat frequencies are considered as the micro vibration driving force.

Our findings expand on Hunt's experiments [38], where they indicated that the characteristics of US backscattered signals are related to the spatial distribution of the scatterers. Therefore, a very small change in the arrangement of scatterers results in substantial variations in the US backscattered signal. As illustrated in Fig. 4, the number and distribution of nuclei in ROIs obtained from benign and cancer tissues are different; the average number of simulated scatterers representing the cell nuclei is 3500 and 12 000 in a 2 mm $\times$ 2 mm ROI, respectively. Similar to Hunt *et al.*, our simulations suggest that these differences in scatterer arrangements are detected by TeUS.

We also compared the classification of simulated tissue using TeUS data with that of a single US frame based on

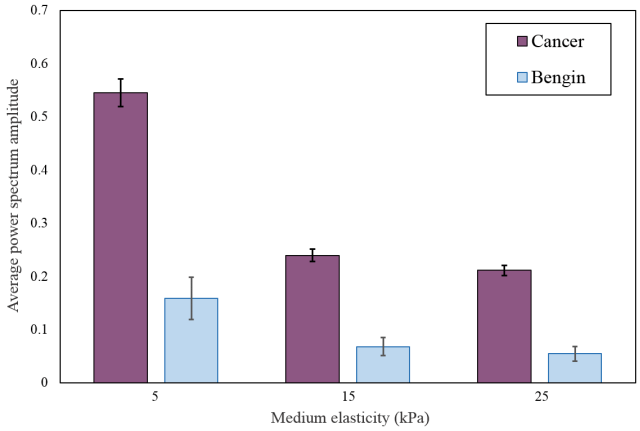

Fig. 10. Distribution of average peak values in the power spectrum at 20 Hz in benign and cancer tissues at elasticities of 5, 15, and 25 kPa.

the approach established by Feleppa *et al.* [49]. Fig. 8(a) shows that the spectral intercept increases as the number of nuclei increases from benign to cancer tissue. A previously established, a theory by Feleppa *et al.* [59] recognizes scatterer number densities as a main contributor to the tissue characterization capability of US spectral analysis, when the acoustic impedance of scatterers in both benign and cancer tissues are identical. Conversely, the differences between spectral slope (LF_S) in benign and cancer tissues were not statistically significant ($p = 0.25$). These results are expected as spectral slope is dependent on scatterer size, which was identical in the two tissues in our simulations [49]. In the context of the simulations performed in the paper, while features suggested by Feleppa *et al.* were partially able to classify the simulated benign and cancer tissues (based on p-values computed in the statistical analysis), features driven from TeUS are more sensitive to the scatterer number and arrangement, and can lead to a more robust classifications of tissue where such differences are present. Considering the limitations of the current simulations, further studies that incorporate the size of the nucleus in addition to its spatial arrangement are required to compare the tissue classification capabilities of TeUS versus spectral analysis of a single RF image.

To study the role of elasticity of the medium in tissue characterization properties of TeUS, we simulated the pathology mimicking phantoms with three elasticities of 5, 15, and 25 kPa. As illustrated in Fig. 10, using TeUS, we can accurately separate benign and cancer tissues irrespective of their corresponding elasticities. In addition, the amplitude of the power spectrum follows our theoretical derivation and is approximately (given the viscosity of the medium) inversely proportional to E. These results also demonstrate that if in conjunction with TeUS imaging, an elastography technique is used to measure the absolute elasticity of tissue, TeUS data can be calibrated to develop an elasticity independent tissue characterization approach.

Our simulations in this paper are restricted to point scatterers. Further studies are required to incorporate more extensive representation of tissue microanatomical structure, which includes considering the effect of scatterer size, specifically in cancerous tissue with higher Gleason score, on the back scatterered RF signal [1], [60]. The capability of TeUS for tissue classification is, however, expected to be unaffected since nuclei are considered to be a dominant scattering source to US propagating waves at many imaging frequencies. Furthermore, the mechanical and US simulations presented in this paper do not consider the structural inhomogeneity of the tissue, which also needs to be included in the future work. Other potential simulations may embrace various mechanical pulsation sources in the medium to mimic capillaries and major vessels surrounding the tissue of interest.

REFERENCES

[1] M. L. Oelze and J. Mamou, "Review of quantitative ultrasound: Envelope statistics and backscatter coefficient imaging and contributions to diagnostic ultrasound," *IEEE Trans. Ultrason., Ferroelect., Freq. Control*, vol. 63, no. 2, pp. 336–351, Feb. 2016.

[2] J. Mamou and M. L. Oelze, *Quantitative Ultrasound in Soft Tissues*. Amsterdam, The Netherlands: Springer, 2013.

[3] E. D. Nelson, C. B. Slotoroff, L. G. Gomella, and E. J. Halpern, "Targeted biopsy of the prostate: The impact of color Doppler imaging and elastography on prostate cancer detection and Gleason score," *Urology*, vol. 70, no. 6, pp. 1136–1140, 2007.

[4] S. W. Xie *et al.*, "Influence of serum prostate-specific antigen (PSA) level, prostate volume, and PSA density on prostate cancer detection with contrast-enhanced sonography using contrast-tuned imaging technology," *J. Ultrasound Med.*, vol. 32, no. 5, pp. 741–748, 2013.

[5] S. M. Han, H. J. Lee, and J. Y. Choi, "Computer-aided prostate cancer detection using texture features and clinical features in ultrasound image," *J. Digit. Imag.*, vol. 21, no. 1, pp. 121–133, 2008.

[6] P.-H. Tsui and C.-C. Chang, "Imaging local scatterer concentrations by the nakagami statistical model," *Ultrasound Med. Biol.*, vol. 33, no. 4, pp. 608–619, 2007.

[7] E. J. Feleppa, C. R. Porter, J. A. Ketterling, S. Dasgupta, S. Ramachandran, and D. Sparks, "Recent advances in ultrasonic tissue-type imaging of the prostate," *Acoustical Imaging*, vol. 28. Dordrecht, The Netherlands: Springer, 2007, pp. 331–339.

[8] F. L. Lizzi, M. Ostromogilsky, E. J. Feleppa, M. C. Rorke, and M. M. Yaremko, "Relationship of ultrasonic spectral parameters to features of tissue microstructure," *IEEE Trans. Ultrason., Ferroelect., Freq. Control*, vol. UFFC-34, no. 3, pp. 319–329, May 1986.

[9] J. Mamou, M. L. Oelze, W. D. O'Brien, Jr., and J. F. Zachary, "Identifying ultrasonic scattering sites from three-dimensional impedance maps," *J. Acoust. Soc. Amer.*, vol. 117, no. 1, pp. 413–423, 2005.

[10] R. M. Vlad, S. Brand, A. Giles, M. C. Kolios, and G. J. Czarnota, "Quantitative ultrasound characterization of responses to radiotherapy in cancer mouse models," *Clin. Cancer Res.*, vol. 15, no. 6, pp. 2067–2075, 2009.

[11] L. Zhai *et al.*, "Acoustic radiation force impulse imaging of human prostates *ex vivo*," *Ultrasound Med. Biol.*, vol. 36, no. 4, pp. 576–588, 2010.

[12] S. E. Salcudean, D. French, S. Bachmann, R. Zahiri-Azar, X. Wen, and W. J. Morris, "Viscoelasticity modeling of the prostate region using vibro-elastography," in *Medical Image Computing and Computer-Assisted Intervention—MICCAI*. Berlin, Germany: Springer, 2006, pp. 389–396.

[13] J. Ophir *et al.*, "Elastographic imaging," *Ultrasound Med. Biol.*, vol. 26, pp. S23–S29, May 2000.

[14] T. Miyagawa *et al.*, "Real-time elastography for the diagnosis of prostate cancer: Evaluation of elastographic moving images," *Jpn. J. Clin. Oncol.*, vol. 39, no. 6, pp. 394–398, 2009.

[15] W. A. Berg *et al.*, "Shear-wave elastography improves the specificity of breast US: The BE1 multinational study of 939 masses," *Radiology*, vol. 262, no. 2, pp. 435–449, 2012.

[16] M. Moradi *et al.*, "Multiparametric 3D *in vivo* ultrasound vibroelastography imaging of prostate cancer: Preliminary results," *Med. Phys.*, vol. 41, no. 7, pp. 073505-1–073505-12, 2014.

[17] M. Moradi, P. Mousavi, and P. Abolmaesumi, "Tissue characterization using fractal dimension of high frequency ultrasound RF time series," in *Medical Image Computing and Computer-Assisted Intervention—MICCAI*. Berlin, Germany: Springer, 2007, pp. 900–908.

[18] M. Moradi *et al.*, "Discrete Fourier analysis of ultrasound RF time series for detection of prostate cancer," in *Proc. 29th Annu. Int. Conf. IEEE Eng. Med. Biol. Soc. (EMBS)*, Aug. 2007, pp. 1339–1342.

[19] M. Moradi, P. Mousavi, P. A. Isotalo, D. R. Siemens, E. E. Sauerbrei, and P. Abolmaesumi, "A new approach to analysis of RF ultrasound echo signals for tissue characterization: Animal studies," *Proc. SPIE*, vol. 6513, p. 65130P, Mar. 2007.

[20] M. Moradi, P. Abolmaesumi, D. R. Siemens, E. E. Sauerbrei, A. H. Boag, and P. Mousavi, "Augmenting detection of prostate cancer in transrectal ultrasound images using SVM and RF time series," *IEEE Trans. Biomed. Eng.*, vol. 56, no. 9, pp. 2214–2224, Sep. 2009.

[21] F. Imani *et al.*, "Ultrasound-based characterization of prostate cancer using joint independent component analysis," *IEEE Trans. Biomed. Eng.*, vol. 62, no. 7, pp. 1796–1804, Jul. 2015.

[22] F. Imani *et al.*, "Computer-aided prostate cancer detection using ultrasound RF time series: *In vivo* feasibility study," *IEEE Trans. Med. Imag.*, vol. 34, no. 11, pp. 2248–2257, Nov. 2015.

[23] S. Azizi *et al.*, "Detection of prostate cancer using temporal sequences of ultrasound data: A large clinical feasibility study," *Int. J. Comput. Assist. Radiol. Surg.*, vol. 11, no. 6, pp. 947–956, 2016.

[24] M. Moradi, P. Abolmaesumi, and P. Mousavi, "Tissue typing using ultrasound RF time series: Experiments with animal tissue samples," *Med. Phys.*, vol. 37, no. 8, pp. 4401–4413, 2010.

[25] F. Imani *et al.*, "Ultrasound-guided characterization of interstitial ablated tissue using RF time series: Feasibility study," *IEEE Trans. Biomed. Eng.*, vol. 60, no. 6, pp. 1608–1618, Jun. 2013.

[26] S. Azizi *et al.*, "Ultrasound-based detection of prostate cancer using automatic feature selection with deep belief networks," in *Proc. Int. Conf. Med. Image Comput. Comput.-Assist. Intervent*, 2015, pp. 70–77.

[27] M. Moradi, S. S. Mahdavi, G. Nir, E. C. Jones, S. L. Goldenberg, and S. E. Salcudean, "Ultrasound RF time series for tissue typing: First *in vivo* clinical results," *Proc. SPIE*, vol. 8670, pp. 86701I1-1–86701I1-8, Mar. 2013.

[28] A. Khojaste *et al.*, "Characterization of aggressive prostate cancer using ultrasound RF time series," *Proc. SPIE*, vol. 9414, p. 94141A, Mar. 2015.

[29] S. Ghavidel *et al.*, "Classification of prostate cancer grade using temporal ultrasound: *In vivo* feasibility study," *Proc. SPIE*, vol. 9786, p. 97860K, Mar. 2016.

[30] S. Azizi *et al.*, "Classifying cancer grades using temporal ultrasound for transrectal prostate biopsy," in *Proc. Int. Conf. Med. Image Comput. Comput.-Assist. Intervent*, 2016, pp. 653–661.

[31] M. I. Daoud, P. Mousavi, F. Imani, R. Rohling, and P. Abolmaesumi, "Tissue classification using ultrasound-induced variations in acoustic backscattering features," *IEEE Trans. Biomed. Eng.*, vol. 60, no. 2, pp. 310–320, Feb. 2013.

[32] S. Bayat *et al.*, "Tissue mimicking simulations for temporal enhanced ultrasound-based tissue typing," *Proc. SPIE*, vol. 10139, p. 101390D, Mar. 2017.

[33] S. Azizi *et al.*, "Detection and grading of prostate cancer using temporal enhanced ultrasound: Combining deep neural networks and tissue mimicking simulations," *Int. J. Comput. Assist. Radiol. Surg.*, vol. 12, no. 8, pp. 1293–1305, 2017.

[34] J. W. Hunt, A. E. Worthington, A. Xuan, M. C. Kolios, G. J. Czarnota, and M. D. Sherar, "A model based upon pseudo regular spacing of cells combined with the randomisation of the nuclei can explain the significant changes in high-frequency ultrasound signals during apoptosis," *Ultrasound Med. Biol.*, vol. 28, no. 2, pp. 217–226, 2002.

[35] R. M. Vlad, N. M. Alajez, A. Giles, M. C. Kolios, and G. J. Czarnota, "Quantitative ultrasound characterization of cancer radiotherapy effects *in vitro*," *Int. J. Radiation Oncol. Biol. Phys.*, vol. 72, no. 4, pp. 1236–1243, 2008.

[36] G. J. Czarnota and M. C. Kolios, "Ultrasound detection of cell death," *Imag. Med.*, vol. 2, no. 1, pp. 17–28, 2010.

[37] M. L. Oelze, W. D. O'Brien, J. P. Blue, and J. F. Zachary, "Differentiation and characterization of rat mammary fibroadenomas and 4T1 mouse carcinomas using quantitative ultrasound imaging," *IEEE Trans. Med. Imag.*, vol. 23, no. 6, pp. 764–771, Jun. 2004.

[38] J. W. Hunt, A. E. Worthington, and A. T. Kerr, "The subtleties of ultrasound images of an ensemble of cells: Simulation from regular and more random distributions of scatterers," *Ultrasound Med. Biol.*, vol. 21, no. 3, pp. 329–341, 1995.

[39] R. E. Baddour, M. Sherar, J. W. Hunt, G. Czarnota, and M. C. Kolios, "High-frequency ultrasound scattering from microspheres and single cells," *J. Acoust. Soc. Amer.*, vol. 117, no. 2, pp. 934–943, 2005.

[40] G. Czarnota *et al.*, "Ultrasound imaging of apoptosis: High-resolution non-invasive monitoring of programmed cell death *in vitro, in situ* and *in vivo*," *Brit. J. Cancer*, vol. 81, no. 3, pp. 520–527, 1999.

[41] M. C. Kolios, G. J. Czarnota, M. Lee, J. W. Hunt, and M. D. Sherar, "Ultrasonic spectral parameter characterization of apoptosis," *Ultrasound Med. Biol.*, vol. 28, no. 5, pp. 589–597, 2002.

[42] T. E. Doyle, K. H. Warnick, and B. L. Carruth, "Histology-based simulations for the ultrasonic detection of microscopic cancer *in vivo*," *J. Acoust. Soc. Amer.*, vol. 122, no. 6, pp. EL210–EL216, 2007.

[43] M. I. Daoud and J. C. Lacefield, "Stochastic modeling of normal and tumor tissue microstructure for high-frequency ultrasound imaging simulations," *IEEE Trans. Biomed. Eng.*, vol. 56, no. 12, pp. 2806–2815, Dec. 2009.

[44] M. I. Daoud and J. C. Lacefield, "Three-dimensional computer simulation of high-frequency ultrasound imaging of healthy and cancerous murine liver tissues," *Proc. SPIE*, vol. 7968, pp. 79680H-1–79680H-7, Mar. 2011.

[45] R. K. Saha and M. C. Kolios, "Effects of cell spatial organization and size distribution on ultrasound backscattering," *IEEE Trans. Ultrason., Ferroelect., Freq. Control*, vol. 58, no. 10, pp. 2118–2131, Oct. 2011.

[46] E. Franceschini, R. Guillermin, F. Tourniaire, S. Roffino, E. Lamy, and J.-F. Landrier, "Structure factor model for understanding the measured backscatter coefficients from concentrated cell pellet biophantoms," *J. Acoust. Soc. Amer.*, vol. 135, no. 6, pp. 3620–3631, 2014.

[47] A. Han and W. D. O'Brien, "Structure function: Theory, ultrasonic measurement, and histology," in *Proc. IEEE Int. Ultrason. Symp. (IUS)*, Oct. 2015, pp. 1–4.

[48] J. Jensen, "A model for the propagation and scattering of ultrasound in tissue," *J. Acoust. Soc. Amer.*, vol. 89, no. 1, pp. 182–191, 1991.

[49] E. J. Feleppa *et al.*, "Typing of prostate tissue by ultrasonic spectrum analysis," *IEEE Trans. Ultrason., Ferroelect., Freq. Control*, vol. 43, no. 4, pp. 609–619, Jul. 1996.

[50] M. L. Oelze and W. D. O'Brien, Jr., "Method of improved scatterer size estimation and application to parametric imaging using ultrasound," *J. Acoust. Soc. Amer.*, vol. 112, no. 6, pp. 3053–3063, 2002.

[51] O. Mattausch and O. Goksel, "Image-based PSF estimation for ultrasound training simulation," in *Proc. Int. Workshop Simulation Synth. Med. Imag.*, 2016, pp. 23–33.

[52] M. Zhang *et al.*, "Quantitative characterization of viscoelastic properties of human prostate correlated with histology," *Ultrasound Med. Biol.*, vol. 34, no. 7, pp. 1033–1042, 2008.

[53] V. Chan and A. Perlas, "Basics of ultrasound imaging," in *Atlas of Ultrasound-Guided Procedures in Interventional Pain Management*. New York, NY, USA: Springer, 2011, pp. 13–19.

[54] K. A. Iczkowski *et al.*, "Digital quantification of five high-grade prostate cancer patterns, including the cribriform pattern, and their association with adverse outcome," *Amer. J. Clin. Pathol.*, vol. 136, no. 1, pp. 98–107, 2011.

[55] M. Doyley, "Model-based elastography: A survey of approaches to the inverse elasticity problem," *Phys. Med. Biol.*, vol. 57, no. 3, p. R35, 2012.

[56] S. Li *et al.*, "A feasibility study of MR elastography in the diagnosis of prostate cancer at 3.0T," *Acta Radiol.*, vol. 52, no. 3, pp. 354–358, 2011.

[57] W. C. Carson, G. J. Gerling, T. L. Krupski, C. G. Kowalik, J. C. Harper, and C. A. Moskaluk, "Material characterization of *ex vivo* prostate tissue via spherical indentation in the clinic," *Med. Eng. Phys.*, vol. 33, no. 3, pp. 302–309, 2011.

[58] F. Imani *et al.*, "Augmenting MRI–transrectal ultrasound-guided prostate biopsy with temporal ultrasound data: A clinical feasibility study," *Int. J. Comput. Assist. Radiol. Surg.*, vol. 10, no. 6, pp. 727–735, 2015.

[59] E. J. Feleppa, F. L. Lizzi, D. J. Coleman, and M. M. Yaremko, "Diagnostic spectrum analysis in ophthalmology: A physical perspective," *Ultrasound Med. Biol.*, vol. 12, no. 8, pp. 623–631, 1986.

[60] J. Mamou *et al.*, "Three-dimensional high-frequency backscatter and envelope quantification of cancerous human lymph nodes," *Ultrasound Med. Biol.*, vol. 37, no. 3, pp. 345–357, 2011.

Authors' photographs and biographies not available at the time of publication.